High-Fidelity Coupled Fluid-Structure Interaction Simulations with Adaptive Meshing

Vivek Ojha[*], Krzysztof J. Fidkowski[†], and Carlos E. S. Cesnik[‡]

Department of Aerospace Engineering, University of Michigan, Ann Arbor, MI 48109, USA

This paper demonstrates an adaptive approach for solving fluid-structure interaction problems using high-fidelity numerical methods. A high-order partitioned approach is applied to couple the fluid and the structural subsystems, where the fluid subsystem is discretized using a discontinuous Galerkin finite-element method, while the structures solver uses a continuous Galerkin discretization. High-order time integration schemes are used by the coupled solver to march forward in time. The space-time mesh of the fluid subsystem is adapted using output-based methods. The error estimates for the unsteady outputs are evaluated by calculating the uncoupled, unsteady adjoint of the fluid subsystem. The benefits of adaptive meshing are showcased on a one-dimensional cantilevered Euler-Bernoulli beam placed in a low-Reynolds number flow and on a two-dimensional pitching-plunging airfoil in a high-Reynolds number flow.

I.   Introduction

Numerical simulation of fluid structure interaction (FSI) is a complex and challenging problem that finds relevance across disciplines. The focus of this paper is on the aeronautical applications of FSI where numerical simulation can be used to improve the understanding and prediction of coupled instabilities observed in aircraft.[1] The interaction between the two systems is non-linear and involves multiple scales, thereby making the coupled system challenging to solve. Many approaches have been suggested for simulating fluid-structure interaction.[2] Numerical approaches for solving the coupled fluid-structure system can be broadly divided into two: monolithic and partitioned. The monolithic approach[3] is a fully-coupled approach where the two systems are solved simultaneously. This approach combines both systems into one large system of equations and solves them simultaneously, which often leads to accurate results but requires significant implementation effort and uses less efficient solvers. The second approach, generally referred to as the partitioned approach, uses two separate solvers to solve the subsystems and then couples them by communication between the solvers. This method facilitates software modularity and mathematical modelling. This work implements a high-order partitioned approach based on the implicit explicit Runge Kutta scheme (IMEX) presented in the work of Van Zuijlen et al,[4] which coupled the two subsystems in a high-order manner without sub-iterations.

The main motivation for developing a high-order FSI solver is to be able to accurately predict coupled outputs like lift, drag and structural deformation. Increasing the accuracy of a simulation by refining the entire space-time mesh makes the simulation computationally expensive and inefficient. A better strategy is to evaluate errors in the output of interest and to adapt the mesh in the regions of space time which contribute most to the error. Such methods are called output-based adaptive methods. They offer a systematic approach for identifying regions of the domain that require more resolution for the prediction of scalar outputs of interest.[5]

In this paper, a high-order fluid structure interaction solver is developed by using a high-order partitioned coupling algorithm. Further, the adaptive techniques are applied to 1D and 2D cases to validate the output-based adaptation strategy, and to demonstrate a reduction in computational cost. The outline of the re-

---

[*]Ph.D. Candidate
[†]Associate Professor, AIAA Senior Member
[‡]Professor, Fellow AIAA

mainder of the paper is as follows. Section II reviews the governing equations of the fluid and structural subsystems. Section III reviews the spatial and temporal coupling algorithm for the partitioned approach. Section IV reviews the error estimation and mesh adaptation strategies used in this work. Finally, Section V outlines the results generated using these methods.

II.   Governing Equations

II.A.   Fluid Subsystem

The fluid subsystem is governed by the Navier-Stokes equations, given by

$$\frac{\partial \mathbf{u}}{\partial t}\Big|_x + \nabla \cdot \vec{\mathbf{F}}(\mathbf{u}, \nabla \mathbf{u}) = \mathbf{0}, \quad \vec{\mathbf{F}} = \vec{\mathbf{F}}^i(\mathbf{u}) - \vec{\mathbf{F}}^\nu(\mathbf{u}, \nabla \mathbf{u}), \tag{1}$$

where $\mathbf{u}(\vec{x}, t) \in \mathbb{R}^s$ is the conservative state vector, $\vec{x} \in \mathbb{R}^d$ is the spatial coordinate, $t \in \mathbb{R}$, and $\vec{\mathbf{F}}^i$ and $\vec{\mathbf{F}}^\nu$ are the inviscid and viscous fluxes, respectively. In the case of a non-deformable domain, the fluid equations are solved numerically in the Eulerian frame of reference, where the computational grid is fixed and the fluid moves with respect to the grid. However, numerical simulation of fluid dynamics involving a deforming domain, such as in the case of FSI, face issues due to the lack of precise interface definition and under-resolved flow features when solved in the Eulerian frame of reference. The Lagrangian approach on the other hand, faces problems dealing with large distortions of the computational domain. To resolve these issues, an alternate method, the Arbitrary Lagrangian Eulerian approach, has been introduced and is applied in the present work.

II.B.   Arbitrary Lagrangian-Eulerian Formulation

The Arbitrary Lagrangian Eulerian (ALE) approach combines advantages of both the Eulerian and Lagrangian approaches. In this method, the deformable physical domain is mapped to a fixed referenced domain by a time dependent mapping. A simple and effective ALE method for DG was introduced by Persson et al[6] and a similar approach is followed in this work.[7]

Let the physical space be defined by v(t) and the reference space by V(t), and let $G(\vec{x}, t)$ represent the one-to-one time-dependent mapping between the two spaces. Each point $\vec{X}$ in the static reference domain is mapped to a corresponding point $\vec{x}(\vec{X}, t)$ in the physical domain, based on the desired deformation of the mesh. The gradient of the mapping, represented by $\mathbf{G}$, and the mapping velocity, $\vec{v}_X$, are given by:

$$\mathbf{G} = \nabla_X G, \quad \vec{v}_X = \frac{\partial G}{\partial t}\Big|_X \tag{2}$$

Let $g = \det(\mathbf{G})$. Thus, the corresponding Navier-Stokes equations in the reference frame can be written as

$$\frac{\partial \mathbf{u}_X}{\partial t}\Big|_X + \nabla_X \cdot \vec{\mathbf{F}}_X(\mathbf{u}_X, \nabla_X \mathbf{u}_X) = \mathbf{0}, \quad \vec{\mathbf{F}}_X = \vec{\mathbf{F}}_X^i(\mathbf{u}_X) - \vec{\mathbf{F}}_X^\nu(\mathbf{u}_X, \nabla_X \mathbf{u}_X), \tag{3}$$

where the transformed vectors, derivatives, and fluxes in the reference frame are given by:

$$\mathbf{u}_X = g\mathbf{u}, \tag{4}$$

$$\nabla_x \mathbf{u} = \nabla_X(g^{-1}\mathbf{u}_X)\mathbf{G}^{-T} = (g^{-1}\nabla_X \mathbf{u}_X - \mathbf{u}_X \nabla_X(g^{-1}))\mathbf{G}^{-T}, \tag{5}$$

$$\vec{\mathbf{F}}_X^i = g\mathbf{G}^{-1}\vec{\mathbf{F}}^i - \mathbf{u}_X \mathbf{G}^{-1}\vec{v}_X, \qquad \vec{\mathbf{F}}_X^\nu = g\mathbf{G}^{-1}\vec{\mathbf{F}}^\nu. \tag{6}$$

II.C.   Spatial Discretization

To discretize the state equations (Eq. 1), a discontinuous Galerkin finite-element method is used in space. DG,[8] as a finite-element method, approximates the state $\mathbf{u}$ in functional form using linear combinations of basis functions on each element. No continuity constraints are imposed between adjacent elements. Denoting

American Institute of Aeronautics and Astronautics

by T_h the set of N_e elements in a non-overlapping tessellation of the domain Ω, the state on element e, Ω_e, is approximated as

$$\mathbf{u}_h(\vec{x}(\vec{\xi}))\Big|_{\Omega_e} = \sum_{n=1}^{N_p} \mathbf{U}_{en}\phi_{en}(\vec{x}(\vec{\xi})). \tag{7}$$

In this equation, N_p is the number of basis functions per element, $\mathbf{U}_{en}$ is the vector of s coefficients for the nth basis function on element e: $\phi_{en}(\vec{x}(\vec{\xi}))$, and s is the state rank. $\vec{x}$ denotes the global coordinates, and $\vec{\xi}$ denotes the reference-space coordinates in a master element. Formally, $\mathbf{u}_h \in \mathbf{\mathcal{V}}_h = [\mathcal{V}_h]^s$, where, if the elements are not curved, $\mathcal{V}_h = \{u \in L_2(\Omega) : u|_{\Omega_e} \in \mathcal{P}^p \ \forall \Omega_e \in T_h\}$, and $\mathcal{P}^p$ denotes polynomials of order p on the element. With the spatial discretization described above, the governing equations can written in an abbreviated form as:

$$\bar{\mathbf{R}}^f = \mathbf{M}^f \frac{\mathrm{d}\mathbf{U}^f}{\mathrm{d}t} - \mathbf{r}^f = \mathbf{0}, \tag{8}$$

where $\mathbf{r}^f$ is the discrete spatial residual vector, $\bar{\mathbf{R}}^f$ is the temporally strong-form unsteady residual, and the f superscript denotes that these equations apply to the fluids subsystem.

II.D.   Structural Subsystem

The structural dynamics are governed by a set of partial differential equations derived on the basis of continuum modelling with an arbitrary constitutive law. For the initial development of the coupled solver, a linear structure model is assumed. Discretizing the governing equations in space using a continuous finite-element method, the semi discrete form of the equation is given by:

$$\mathbf{M}\ddot{\mathbf{u}}^s + \mathbf{C}\dot{\mathbf{u}}^s + \mathbf{K}\mathbf{u}^s = \mathbf{F}, \tag{9}$$

where $\mathbf{u}^s$ represents the vector of displacements, $\mathbf{M}$ is the mass matrix, and $\mathbf{K}$ is the stiffness matrix of the structure. $\mathbf{C}$ denotes the internal or external damping in the structure, and $\mathbf{F}$ represents the vector of external forces acting on the structure. The semi-discrete form can be re-written as a system of two first-order ordinary differential equations:

$$\begin{bmatrix} \mathbf{M} & \mathbf{0} \\ \mathbf{0} & \mathbf{1} \end{bmatrix} \dot{\mathbf{U}}^s + \begin{bmatrix} \mathbf{C} & \mathbf{K} \\ \mathbf{-1} & \mathbf{0} \end{bmatrix} \mathbf{U}^s = \begin{bmatrix} \mathbf{0} \end{bmatrix} \quad \text{where} \quad \mathbf{U}^s = \begin{bmatrix} \dot{\mathbf{u}}^s \\ \mathbf{u}^s \end{bmatrix}, \tag{10}$$

where $\mathbf{1}$ denotes the identity matrix. The governing equations can be written in an abbreviated form as:

$$\bar{\mathbf{R}}^s = \mathbf{M}^s \frac{\mathrm{d}\mathbf{U}^s}{\mathrm{d}t} - \mathbf{r}^s = \mathbf{0}, \tag{11}$$

where $\mathbf{r}^s$ is the discrete spatial residual vector, and $\bar{\mathbf{R}}^s$ is the strong-form unsteady residual. The superscript s denotes that these equations apply to the structures subsystem.

III.   Fluid Structure Coupling

Solving the coupled fluid-structure problem using a high-order partitioned approach intrinsically requires separate high-order solvers for both the fluid and the structural subsystems. The coupling then occurs by communication between the two solvers. The Discontinuous Galerkin (DG) formulation of the Navier-Stokes equations coupled with high-order time stepping schemes such as ESDIRK4/ DIRK4 allows for the solution of the fluid subsystem with high-order accuracy in both space and time. Similarly, high-order elements in the continuous Galerkin formulation of the structural governing equations coupled with high-order time stepping provides us with high-fidelity solutions for the structural subsystem. Thus, development of a high-order partitioned solver comes down to the order of coupling between the subsystems.

III.A.   Spatial Coupling

The partitioned approach for FSI allows us to use a separate mesh discretization for each subsystem which offers the advantage of resolving regions of complex flow in the fluids or large displacement in the structures.

This may result in meshes for the coupled problem which may not coincide at the interface. Thus, a spatial coupling algorithm is required to interpolate interface displacement and velocities from the structural mesh to the fluids and loads from the fluid mesh to the structures. For one-dimensional test cases, cubic splines provide high-order of accuracy for interpolation and have been used for the spatial coupling in this work. When dealing with complex structures for multi-dimensional problems, radial basis function (RBF) or nearest neighbor interpolation will be considered based on previous studies.[9]

III.B. Mesh Deformation

For deforming domains, the ALE formulation of the Navier-Stokes equations requires a mapping between the reference and the deformed physical mesh. An explicit mapping presented by Persson and Peraire[10] for the case of a membrane has been used in this study, where the mapping that deforms the structure according to a given shape reduces to the identity mapping away from the structure and is smooth in-between. The mesh motion algorithm differs slightly from the explicit mapping where 7th order (septic) polynomials instead of quintic polynomials are used to blend in the radial directions.

III.C. IMEX

The time integrator used in this study is the Implicit Explicit Runge Kutta scheme.[11] IMEX is a high-order time integration scheme developed for stiff time marching problems where the velocity term can be split into a stiff and non-stiff component. The stiff component of the velocity is then solved implicitly in time, while the non-stiff component is solved explicitly. To demonstrate the scheme, consider a semi-discretized multiphysics equation,

$$\mathbf{M}\dot{\mathbf{u}} = \mathbf{r}(\mathbf{u}, t) = \mathbf{f}(\mathbf{u}, t) + \mathbf{g}(\mathbf{u}, t), \tag{12}$$

where $\mathbf{M}$ is the mass matrix, $\mathbf{u}$ is the state vector, and $\mathbf{r}$ is the residual which is split into $\mathbf{f}$ and $\mathbf{g}$, the stiff and non-stiff component respectively. $\mathbf{f}$ is integrated with an s-stage explicit Runge-Kutta scheme and $\mathbf{g}$ is integrated with an s-stage diagonally-implicit Runge-Kutta scheme.

$$\mathbf{u}_{n,j} = \mathbf{u}_{n-1} + \sum_{p=1}^{j-1} \hat{a}_{jp}\hat{k}_{n,p} + \sum_{p=1}^{j} a_{jp}k_{n,p} \tag{13}$$

$$\mathbf{M}\hat{k}_{n,j} = \Delta t_n \mathbf{f}(\mathbf{u}_{n,j}, t_{n-1} + \hat{c}_j \Delta t_n) \tag{14}$$

$$\mathbf{M}k_{n,j} = \Delta t_n \mathbf{g}(\mathbf{u}_{n,j}, t_{n-1} + c_j \Delta t_n) \tag{15}$$

$$\mathbf{u}_n = \mathbf{u}_{n-1} + \sum_{p=1}^{s} \hat{b}_p\hat{k}_{n,p} + \sum_{p=1}^{s} b_p k_{n,p} \tag{16}$$

The IMEX scheme considered in this paper consists of an explicit Runge-Kutta (ERK) and a stiffly-accurate explicit, first stage, singly-diagonally implicit Runge-Kutta (ESDIRK) scheme.

III.D. Temporal Coupling

The coupled FSI problem can be represented in the semi-discrete form as

$$\mathbf{M}\dot{\mathbf{u}} = \mathbf{r}(\mathbf{u}), \tag{17}$$

$$\mathbf{u} = \begin{bmatrix} \mathbf{u}^f \\ \mathbf{u}^s \end{bmatrix}, \quad \mathbf{r} = \begin{bmatrix} \mathbf{r}^f(\mathbf{u}^f; \mathbf{z}(\mathbf{u}^s)) \\ \mathbf{r}^s(\mathbf{u}^s; \mathbf{t}(\mathbf{u}^f)) \end{bmatrix}, \quad \mathbf{M} = \begin{bmatrix} \mathbf{M}^f & 0 \\ 0 & \mathbf{M}^s \end{bmatrix}, \tag{18}$$

where $\mathbf{u}$ is a combined vector of the fluid and structural states, and $\mathbf{z}$ and $\mathbf{t}$ denote the terms in the residual responsible for the coupling of the two subsystems. From Eq. 11, the residual of the structural subsystem may be separated as

$$\mathbf{r}^s(\mathbf{u}^s; \mathbf{t}(\mathbf{u}^f)) = \mathbf{r}^{ss}(\mathbf{u}^s) + \mathbf{r}^{sf}(\mathbf{t}(\mathbf{u}^f)) \tag{19}$$

The first term represents the effect of the current structural state, while the second term represents the effect of the traction from the fluid. Since the second term is linear in $\mathbf{t}$, a predicted value of the traction is introduced, $\tilde{\mathbf{t}}$, as presented in Froehle and Persson.[12] Thus, the residual can be re-written as

$$\mathbf{r}^s(\mathbf{u}^s; \mathbf{t}(\mathbf{u}^s)) = \mathbf{r}^s(\mathbf{u}^s; \tilde{\mathbf{t}}) + \mathbf{r}^{sf}(\mathbf{t}(\mathbf{u}^f) - \tilde{\mathbf{t}}). \tag{20}$$

Using the above formulation, Eq. 8 can be split as

$$\mathbf{M}\frac{d\mathbf{u}}{dt} = \begin{bmatrix} 0 \\ \mathbf{r}^{sf}(\mathbf{t}(\mathbf{u}^f) - \tilde{\mathbf{t}}) \end{bmatrix} + \begin{bmatrix} \mathbf{r}^f(\mathbf{u}^f; \mathbf{z}(\mathbf{u}^s)) \\ \mathbf{r}^s(\mathbf{u}^s; \tilde{\mathbf{t}}) \end{bmatrix}. \tag{21}$$

With the introduction of a predictor, the coupled problem has been suitably modified into a form where the high-order IMEX scheme can be applied. As already mentioned, in the IMEX scheme the stiff (first) term is integrated explicitly and the non-stiff (second) term is integrated implicitly in time. However, the scheme differs slightly from IMEX as the evaluation of the explicit terms $\mathbf{r}^{sf}$ is avoided and instead the stage flux is updated for the structure equation using the corrected value of the coupling $\mathbf{t}(\mathbf{u}^f)$. To solve the subsystems implicitly, ESDIRK4, is employed. An explicit traction predictor, proposed by Van Zuijlen et al,[4] for the structural subsystem, at an implicit stage i is given by

$$\tilde{\mathbf{t}} = \sum_{j=1}^{i-1} \frac{\hat{a}_{ij} - a_{ij}}{a_{ii}} \mathbf{t}_j, \tag{22}$$

where $\hat{a}_{ij}$ and $a_{i,j}$ are the coefficients of the explicit and implicit Runge-Kutta integration schemes.

Figure 1 summarizes a single time step of the coupled solver. The coupled FSI problem uses a block Gauss-Seidel partitioning, where the structural subsystem uses the explicit traction predictor (Step 1) and is integrated first, in an implicit manner (Step 2) . The spatial coupling algorithms transfer the predicted interface data to the fluid subsystem (Step 3) which is then implicitly integrated (Step 4). Corrected traction obtained from the fluid solve is lastly used to correct the structural subsystem (Steps 5 and 6).

IV. Output-Based Mesh Adaptation

In the coupled FSI problem, the numerical error in the output results from discretization errors generated in both the fluid and structural subsystems. For this study, the errors generated in the structural subsystem are neglected and only the errors from the fluid discretization drive the adaptation process. To adapt the mesh, spatially discrete but continuous in time adjoints are used to estimate the error in the output of interest.[13]
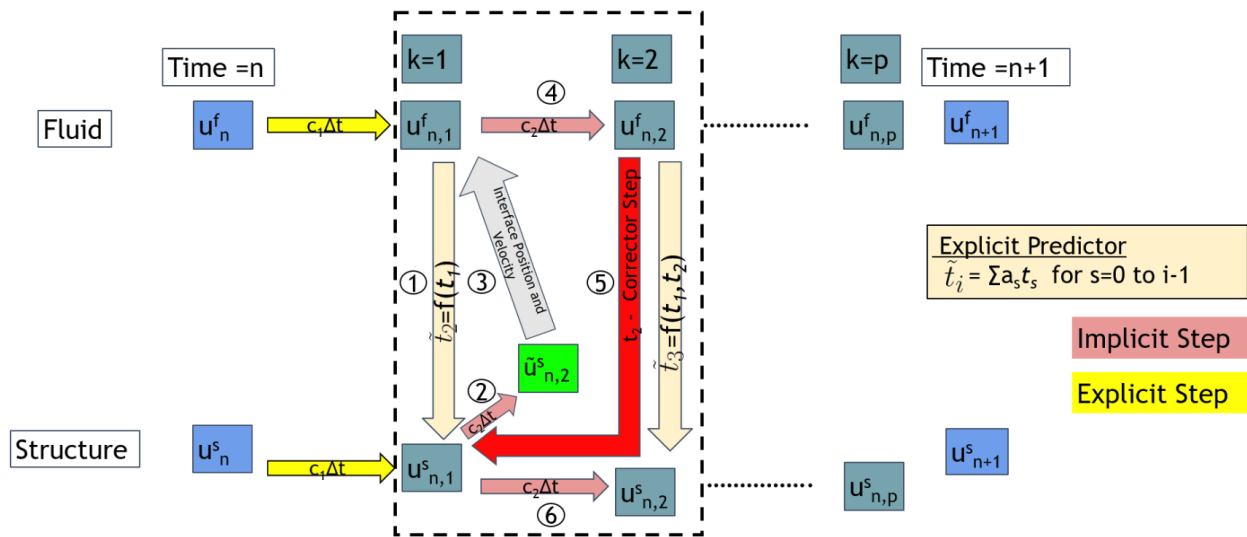

Figure 1. IMEX algorithm for one coupled time step.

American Institute of Aeronautics and Astronautics

IV.A.   Continuous-in-Time Adjoint Evaluation

Consider an unsteady output of the form

$$\bar{J} = \int_0^T J(\mathbf{U}^f, \mathbf{U}^s, t) \; dt, \tag{23}$$

where J is a spatial functional of the fluid, $\mathbf{U}^f$, and structural, $\mathbf{U}^s$, state. The continuous adjoints, $\boldsymbol{\Psi}_f$ and $\boldsymbol{\Psi}_s$, represent the sensitivity of the output to perturbations in the unsteady residuals $\bar{\mathbf{R}}^f$ (Eq. 8) and $\bar{\mathbf{R}}^s$ (Eq. 11), respectively. To derive the adjoint equations, a Lagrangian is defined as

$$\mathcal{L} = \bar{J} + \int_0^T \boldsymbol{\Psi}_f^T \bar{\mathbf{R}}^f dt + \int_0^T \boldsymbol{\Psi}_s^T \bar{\mathbf{R}}^s dt. \tag{24}$$

As the focus of this work is on the errors in the fluid discretization and thus the fluid adjoint, perturbations in the structural state are ignored and assumed to be independent of the perturbation in the fluid state. Substituting Eq. 23 into Eq. 24, integrating the second term by parts, and requiring stationarity of the Lagrangian with respect to the permissible state variations, which in this particular work is only in the fluid state, $\delta \mathbf{U}^f$, gives

$$\boldsymbol{\Psi}_f^T \mathbf{M}^f \delta \mathbf{U}^f \Big|_{t=T} - \boldsymbol{\Psi}_f^T \mathbf{M}^f \delta \mathbf{U}^f \Big|_{t=0} + \int_0^T \left[\frac{\partial J}{\partial \mathbf{U}^f} - \frac{\mathrm{d} \boldsymbol{\Psi}_f^T}{\mathrm{d}t} \mathbf{M}^f - \boldsymbol{\Psi}_f^T \frac{\partial \mathbf{r}^f}{\partial \mathbf{U}^f} \right] \delta \mathbf{U}^f dt = \mathbf{0}. \tag{25}$$

The middle term at $t = 0$ drops out since the initial condition on the primal fully constrains the state there, so $\delta U^f = 0$ at $t = 0$. The remaining terms yield the adjoint differential equation (from the time integrand, transposed),

$$-\mathbf{M}^f \frac{\mathrm{d} \boldsymbol{\Psi}_f}{\mathrm{d}t} - \frac{\partial \mathbf{r}^{f\,T}}{\partial \mathbf{U}^f} \boldsymbol{\Psi}_f + \frac{\partial J^T}{\partial \mathbf{U}^f} = \mathbf{0}, \tag{26}$$

and the terminal condition

$$\boldsymbol{\Psi}_f(T) = \mathbf{0}. \tag{27}$$

Due to the terminal condition, the adjoint equation is solved backward in time. The time integration scheme used for both the primal and the adjoint equation for this study is ESDIRK4 but other time schemes can be used as well.

IV.B.   Error Estimation

The unsteady adjoint can be used to evaluate the error in the output of interest through the adjoint-weighted residual.[14] Let $\mathbf{U}_H^f$ be the approximate fluid solution obtained from the current space-time approximation space denoted by subscript H and $\boldsymbol{\Psi}_{f,h}^T$ be the fluid adjoint in the fine space denoted by h. The error in the output is defined as:

$$\delta J = J_H(\mathbf{U}_H^f) - J_h(\mathbf{U}_h^f) \approx \frac{\partial J_h}{\partial \mathbf{U}_h^f} \delta \mathbf{U}_h^f \approx -\int_0^T \boldsymbol{\Psi}_{f,h}^T \bar{\mathbf{R}}_h^f(\mathbf{U}_H^f) dt, \tag{28}$$

where $\delta \mathbf{U}_h^f = \mathbf{U}_h^{f,H} - \mathbf{U}_h^f$ is the primal error in the fluid state and $\mathbf{U}_h^{f,H}$ is the injected solution from space H to h. The exact unsteady adjoint, which is unavailable, is approximated in a finer space grid by increasing the degrees of freedom in the spatial discretization.

IV.C.   Mesh Adaptation

Unsteady error estimates in the space-time fluid mesh guide the adaptation process. Space-time elements selected for refinement or coarsening are decided by two factors: 1) estimated error in the space-time element, 2) computational cost of refinement. These two aspects are combined into an adaptive indicator called the

"figure of merit" which is the element error eliminated by refinement divided by the degrees of freedom introduced by the refinement. The cost is defined by the total degrees of freedom,

$$C \equiv C^{\text{space}} C^{\text{time}} \quad , \quad C^{\text{space}} \equiv \sum_{e=1}^{N_e} n(p_e) \quad , \quad C^{\text{time}} \equiv N_t n_r, \tag{29}$$

where $n(p_e)$ is the number of spatial degrees for an element of order p_e, and n_r is the number of temporal degrees of freedom, i.e. system solves, per time step. For example, ESDIRK4 has $n_r = 5$. In this work the adaptive strategy refines in space by hanging node refinement (h-adaptation) or spatial order refinement (p-adaptation) and in time by reducing the uniform time step.

V.   Results

In this section, the high-order coupled solver is validated and the effectivity of the error estimate and the efficiency of the adapted space-time meshes are demonstrated. The two test cases chosen to showcase the benefits of adaptivity in aeroelastic problems are accurate drag estimation on a cantilevered beam subjected to a low Reynolds number flow, and accurate flutter prediction on a pitching-plunging airfoil in a high Reynolds number flow.

V.A.   Cantilevered beam

Consider the flow around an Euler-Bernoulli beam cantilevered at the leading edge. At the undeformed strain-free position, the beam makes an angle of attack of 5 degrees to the flow. The actual beam is considered two dimensional when represented in the fluid mesh, with a length of 1 and a thickness of 0.005. The fluid mesh uses a structured grid consisting of 1954 nodes and 1840 quadrilateral elements. The domain consists of a rectangular box , $[0,9] \times [0,8]$ where the beam is cantilevered at the center of the domain and the fluid enters the domain from the left. Symmetry boundary conditions at the top and bottom of the domain and a static pressure boundary condition at the outlet are used. Figure 2 shows the computational fluid mesh. The one-dimensional beam is represented by 8 beam elements of uniform size in the structures solver. The fluid and structural meshes are constructed such that the interface nodes coincide, thus reducing the error in the structural coupling of the two subsystems. After adaptation, cubic splines are used as the spatial coupling algorithm to transfer data between the subsystems.

The fluid flow properties are Mach number $M = 0.2$ and Reynolds number $Re = 2000$, and the beam has an elastic modulus $E = 0.2$, area moment of inertia $I = 1$, $\rho = 1$, cross section area $A = 1$, and Rayleigh damping parameters, $\alpha = 1$ and $\beta = 1$. At time $t = 0$, the structure is at rest and the fluid state is obtained from a steady solve for the steady state solution of the fluid. $p = 1$ order polynomials have
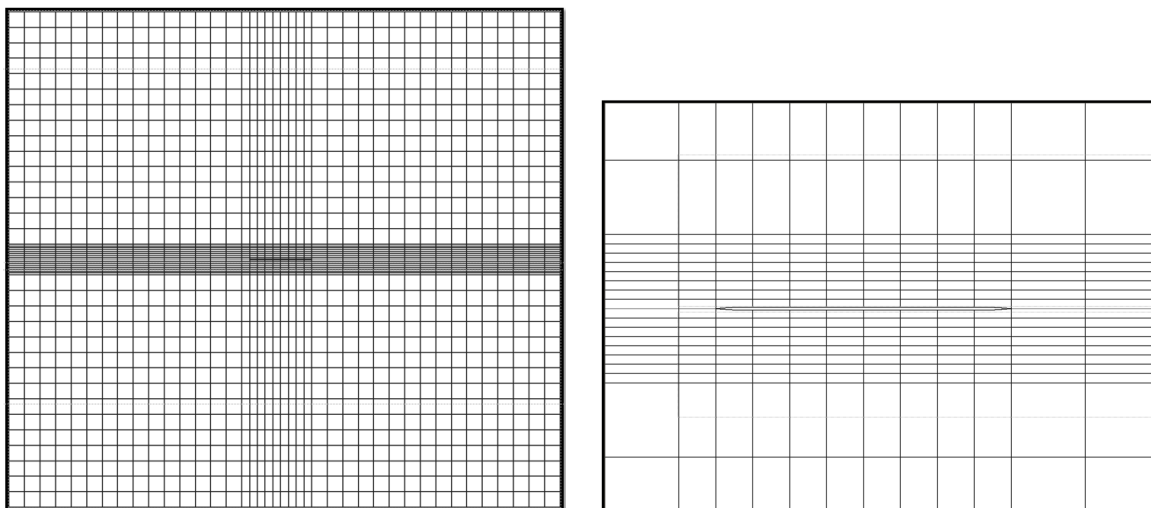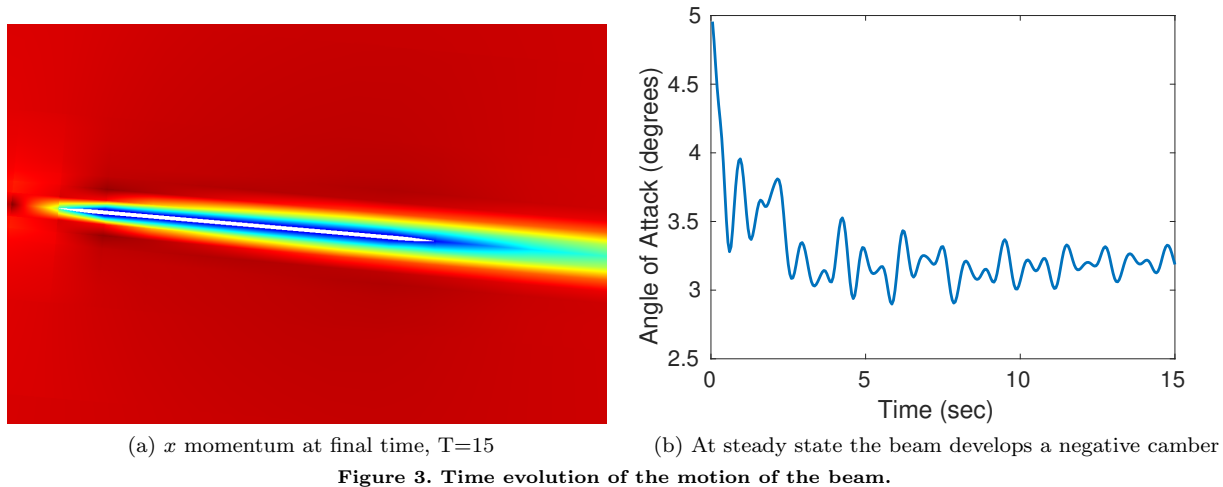

Figure 2. The reference fluid mesh for the cantilevered beam test case.

American Institute of Aeronautics and Astronautics

(a) x momentum at final time, T=15

(b) At steady state the beam develops a negative camber

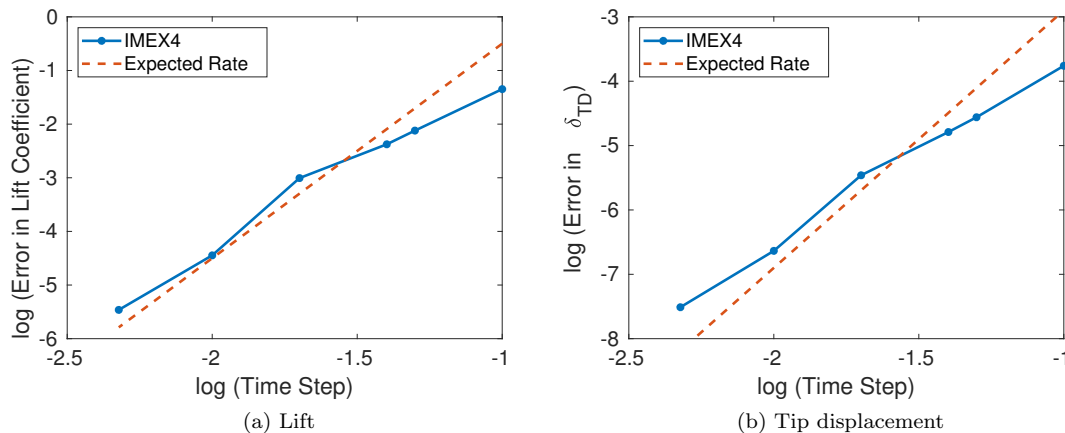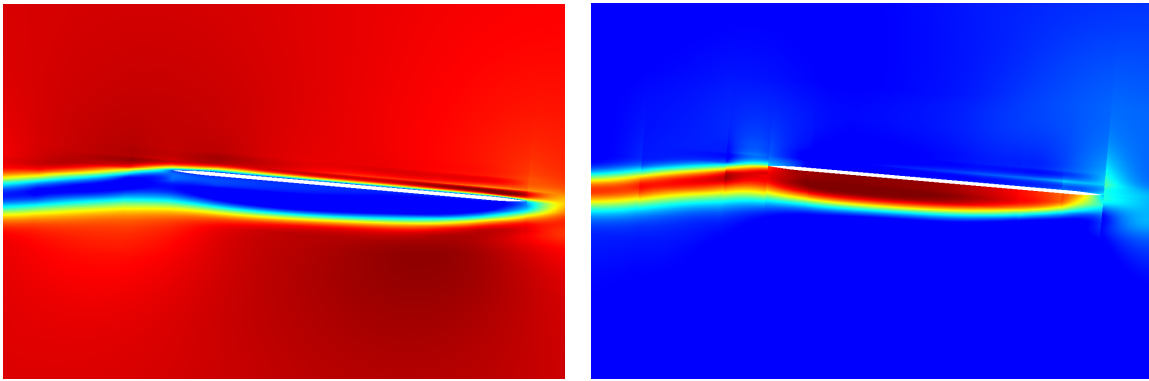Figure 3. Time evolution of the motion of the beam.

been used for the fluid spatial discretization and the time scheme for both subsystems is ESDIRK4. The two subsystems are coupled temporally using the IMEX scheme. For this flow condition, a convex nature in the beam shape is expected at steady state, which is corroborated by Figure 3a, where the final time is $T = 15$. Figure 3b presents the evolution of the angle of attack on the beam over time for this flow condition.

To validate the temporal convergence of the high-order coupled solver, the relative error in the lift coefficient and non-dimensionalized tip displacement are measured at the final time, $T = 4$. A plot of the observed relative error as a function of timestep for the ESDIRK4 scheme is shown in Figure 4. Note that in each case, the scheme exhibits convergence at the designed rate. The plot demonstrates that this partitioned approach attains up to 4th order accuracy in time with the IMEX coupling scheme. The output of interest for mesh adaptation is the time-integral of the drag force on the beam,

$$\bar{J} = \int_{0}^{T} D(t)dt. \tag{30}$$

Figure 5 shows the adjoint solution at the initial time of the simulation. The adjoint solution shows the sensitivity of the output to the perturbation in x-momentum and energy conservation equations. Using the drag adjoint, an unsteady error estimate on the output was evaluated and used to adapt the fluid mesh. Figure 6 compares the output convergence of the drag, using the current adjoint-based approach, to uniform refinement. At every stage of uniform refinement, the spatial degrees of freedom of the fluid computational

(a) Lift

(b) Tip displacement

Figure 4. Convergence study for the IMEX scheme.

American Institute of Aeronautics and Astronautics

<div style="text-align:center">

(a) x-momentum adjoint   (b) Energy adjoint

Figure 5. Uncoupled drag adjoint solution for the beam test case at initial time.

</div>

mesh and the number of time steps are doubled. The growth factor for the total number of space-time degrees of freedom per adaptive iteration is set to $f_{tot}= 2$. The initial solution, on which adaptation takes place, is obtained with $p = 1$ order polynomial, 40 time steps, and a final time of $T = 4$. The plot shows effectiveness of the drag adjoint relative to uniform refinement. The adapted meshes converge to a lower error with fewer degrees of freedom, thereby increasing accuracy and reducing computational cost. Figure 15 shows the adapted fluid mesh after each successive adaptive iteration. The adaptive iterations refine the regions close to the interface of the beam, where the drag adjoint is high, thereby reducing the spatial discretization error in the fluid mesh on the output.

V.B. Two-dimensional pitching plunging NACA 0012 airfoil

A two-dimensional pitching plunging airfoil is a common aeroelastic model which has been studied extensively.[15] The two degree-of-freedom system, when exposed to an airstream of Mach number M_f, exhibits a dynamic instability known as flutter where the two structural modes, pitch and plunge, coalesce, resulting in a sustained simple harmonic motion of the structure. The Mach number M_f, represents the neutral boundary for the system, above which the oscillations became unstable.

To study the phenomenon of flutter, consider a NACA 0012 airfoil pinned at the elastic axis in a free-stream flow of Mach number M_∞ as shown in Figure 7. The two degrees of freedom of the airfoil are the plunge h, which is taken to be positive in the downward direction, and the pitch angle α, which is considered positive clockwise (pitch up). The geometric properties of the airfoil are the chord c and semi-chord b. Measured from the nose of the airfoil, the center of mass and the elastic axis are located at x_{cg} and x_f
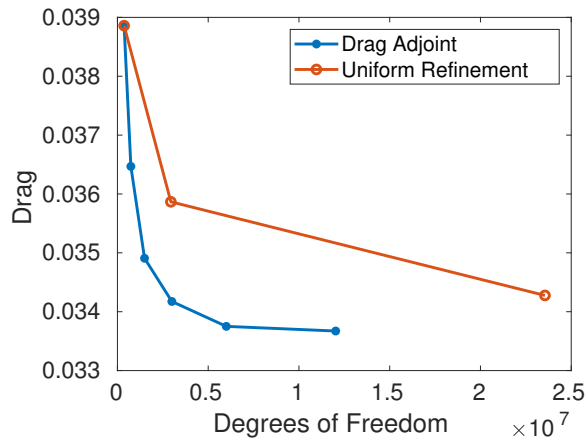

<div style="text-align:center">

Figure 6. Comparison of output-based adaption to uniform refinement.

</div>

<div style="text-align:center">

9 of 16

American Institute of Aeronautics and Astronautics
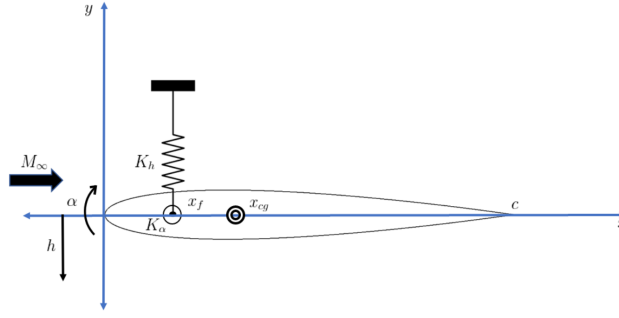
</div>

Figure 7. Model of a two-degree-of-freedom pitching-plunging airfoil

respectively. The inertia properties of the airfoil are the mass, m, and the moment of inertia about the elastic axis, I_f. The airfoil is connected to two springs at the elastic axis where the plunge spring represents the bending stiffness, K_h, of the structure, and the torsional spring represents the torsional stiffness, K_α. The equations of motion of the pitching-plunging airfoil are given as:

$$m\ddot{\mathbf{h}} + S\ddot{\boldsymbol{\alpha}} + K_h\mathbf{h} = -L, \tag{31}$$

$$S\ddot{\mathbf{h}} + I_f\ddot{\boldsymbol{\alpha}} + K_\alpha\boldsymbol{\alpha} = M, \tag{32}$$

where S is the static unbalance defined by the product between $(x_{cg} - x_f)$ and the mass of the airfoil, L is the total lift acting on the airfoil and M is the net moment on the airfoil about the elastic axis. The non-dimensional parameters used to describe the model are defined as:

$$\mu = \frac{m}{\pi \rho_\infty b^2}, \quad \bar{\omega} = \frac{\omega_h}{\omega_\alpha}, \quad r_\alpha = \sqrt{\frac{I_f}{mb^2}}, \quad \chi = \frac{S}{mb}, \tag{33}$$

where μ is the mass ratio, $\bar{\omega}$ is the ratio of the uncoupled natural frequencies, and r_α and χ are the non-dimensional inertia and static balance, respectively. The natural pitching and plunging frequency are defined as $\omega_h = \sqrt{K_h/m}$ and $\omega_\alpha = \sqrt{K_\alpha/I_f}$. The case setup has been taken from Sanchez et al.[16] where the non-dimensional parameters are set as $\mu = 100$, $\bar{\omega} = 0.3185$, $r_\alpha = 0.5$ and $\chi = 0.25$, to ensure a subsonic flutter. The pitching frequency is set to be $\omega_\alpha = 45\text{rad/s}$ and the elastic axis is located at the quarter chord of the
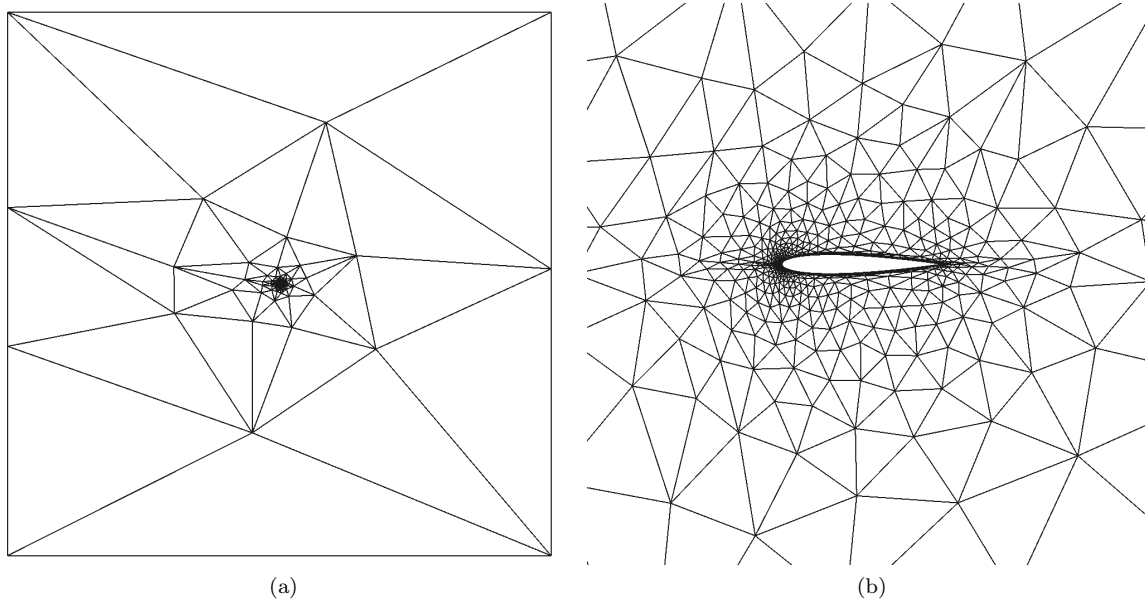

(a)   (b)

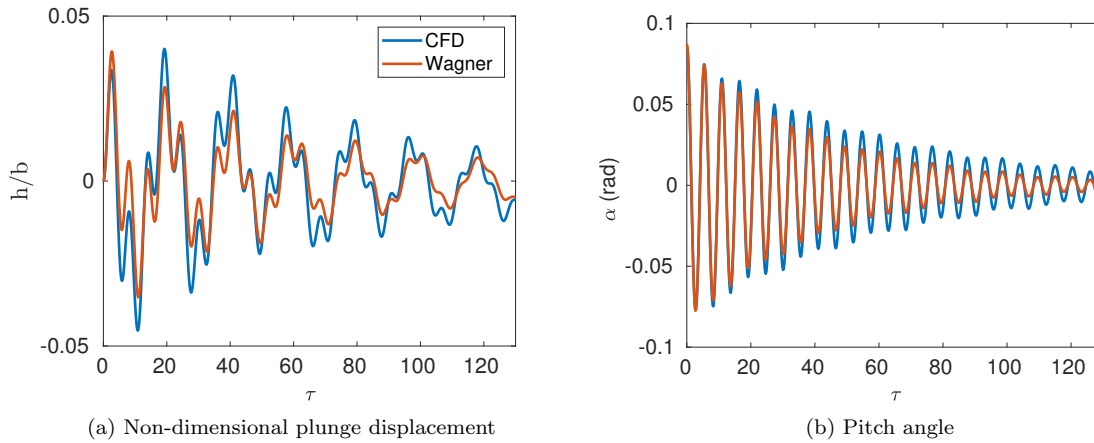**Figure 8. Unstructured viscous mesh for the pitching plunging airfoil,**

American Institute of Aeronautics and Astronautics

(a) Non-dimensional plunge displacement

(b) Pitch angle

Figure 9. Aeroelastic response of the airfoil in the subcritical regime as a function of the non-dimensional time (τ).

airfoil. The Reynolds number is set to $Re = 4 \times 10^6$ and the chord is, c=1. The airfoil is set at an initial angle of attack of five degrees to the flow.

A coarse, unstructured, triangular, viscous mesh of 2766 elements is generated for the coupled simulation, as shown in Figure 8. The airfoil is located centrally in the domain, the boundary of which consists of a square box which spans from [-100c, 100c] in both dimensions. The fluid flow is simulated using a RANS solver with the SA turbulence model.[17] The coupled system uses the fourth-order time scheme, ESDIRK4, introduced in the section III, to march forward in time. A steady-state flow solution is used as the initial condition for the simulation. A mesh motion algorithm is applied to handle the deformations occurring in the fluid subsystem due to the moving airfoil. The mesh motion algorithm divides the spatial domain into two sub-domains. The region extending up to a radial distance of one chord away from the elastic axis is deformed rigidly according to the deformation provided by the structures solver. Following the region of rigid deformation, a septic polynomial blends the deformation smoothly in the region extending between a radial distance of one chord and ten chords resulting in zero deformation at a radial distance of ten chords .

Using the parameters defined above, the aeroelastic response of the coupled system is verified by conducting a simulation at a subcritical Mach number, $M_\infty = 0.1$. The simulation is performed with $p = 3$ order polynomials for the fluid spatial discretization and 60 time steps per oscillation of the plunge mode of the airfoil. The response of the coupled system is compared against Wagner's incompressible aerodynamic model. Figure 9 shows the non-dimensionalized unsteady pitch and plunge displacements as functions of the non-dimensional time, $\tau = \omega_\alpha t$. The unsteady pitch and plunge displacements are consistent with the
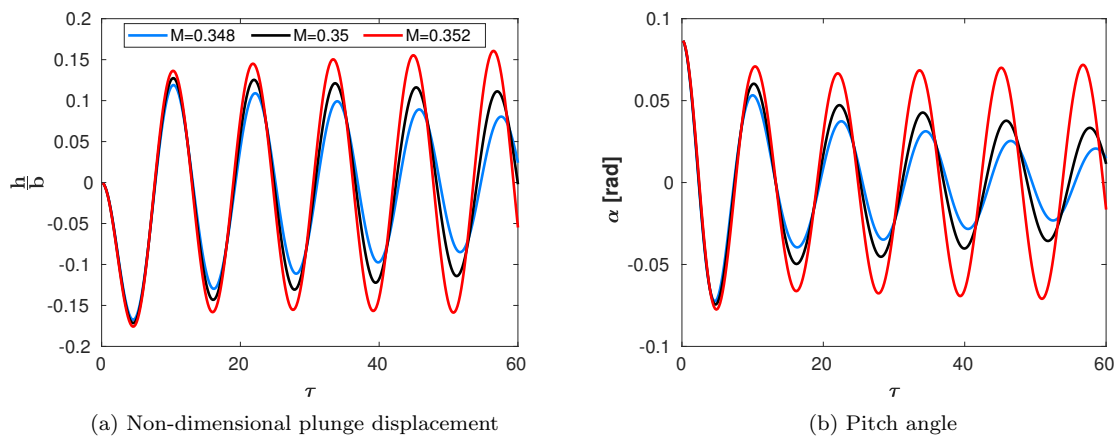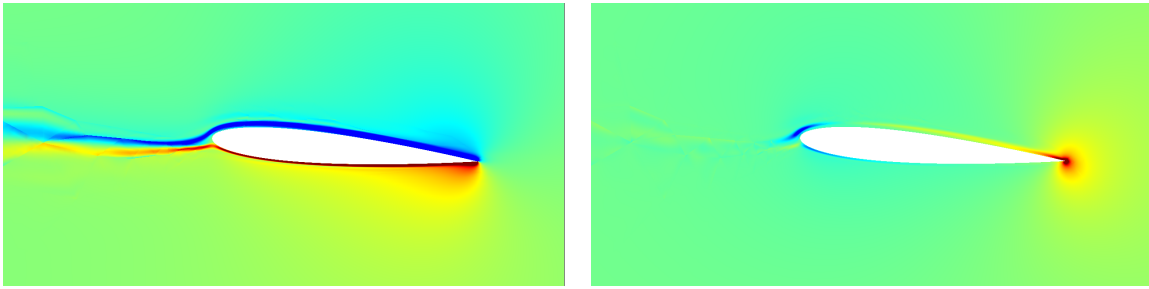

(a) Non-dimensional plunge displacement

(b) Pitch angle

Figure 10. Aeroelastic response of the airfoil near the flutter boundary as a function of the non-dimensional time (τ).

American Institute of Aeronautics and Astronautics

(a) Conservation of the x-momentum adjoint   (b) Conservation of the y-momentum adjoint

Figure 11. Uncoupled lift adjoint solution for the airfoil at the initial time.

theoretical aerodynamics model at the subcritical Mach number as well as other CFD solvers as shown in Sanchez et al.[16] To determine the flutter boundary of the system, the aeroelastic response is recorded for varying Mach numbers. The damping coefficient of the plunge displacement in each run is evaluated by the logarithmic decrement approach and fitted by a quadratic polynomial to estimate the actual flutter Mach number. Figure 10 shows the aeroelastic response at three different Mach numbers close to flutter using $p = 3$ order polynomials for the spatial discretization. The responses at M_∞=0.345 and M_∞=0.348 lie in the sub-critical regime while the response at M_∞=0.352 is past the flutter boundary as the states grow without bound over time. The flutter Mach number is estimated to be at M_f=0.351 by interpolating using the damping evaluated at these Mach numbers.

The errors in the flutter boundary evaluation arise due to the spatial discretization errors in the fluid subsystem and the temporal discretization in both the fluid and the structural subsystem. A p-refinement study of the coupled simulation corroborated the effects of spatial discretization on the flutter boundary for the two-degree of freedom system. An equivalent time-refinement study did not result in a significant change in the flutter boundary due to the fourth-order order time scheme, ESDIRK4, and a small time step used in the coupled simulation. Therefore, the spatial discretization errors dominate the flutter boundary evaluation and an adaptive procedure is used to obtain an optimized fluid mesh.

The current implementation of the adaptation process allows for adaptation in the spatial order of ele-

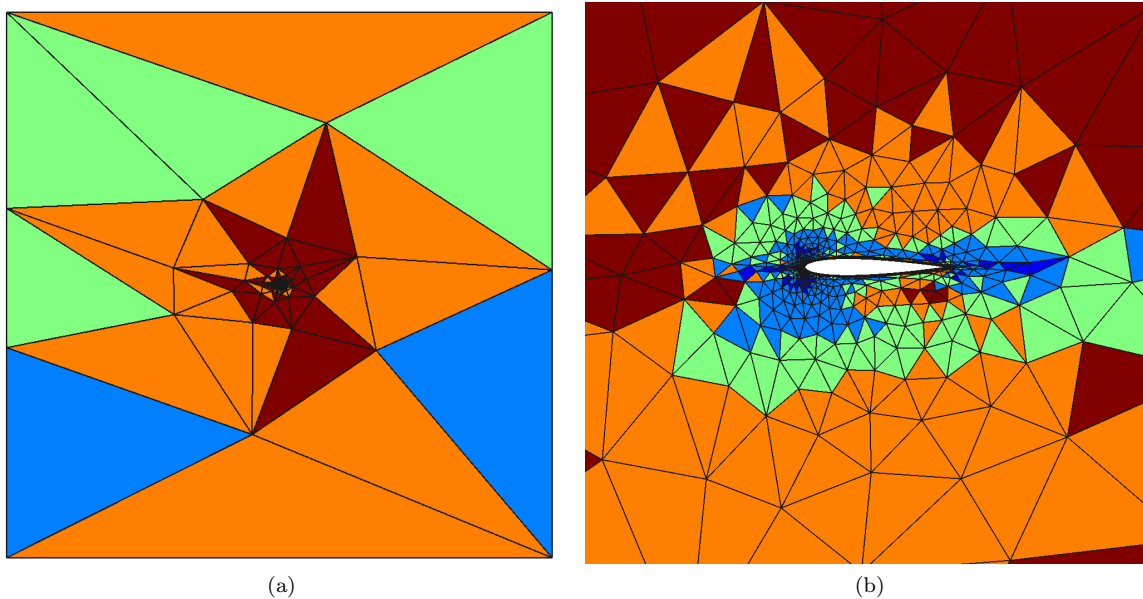(a)   (b)

Figure 12. Element order distribution at the end of the adaptation process on the pitching-plunging airfoil. The elements colored dark blue denote $p = 1$, light blue denote $p = 2$, green denote $p = 3$, orange denote $p = 4$, and dark red denote $p = 5$ order elements.
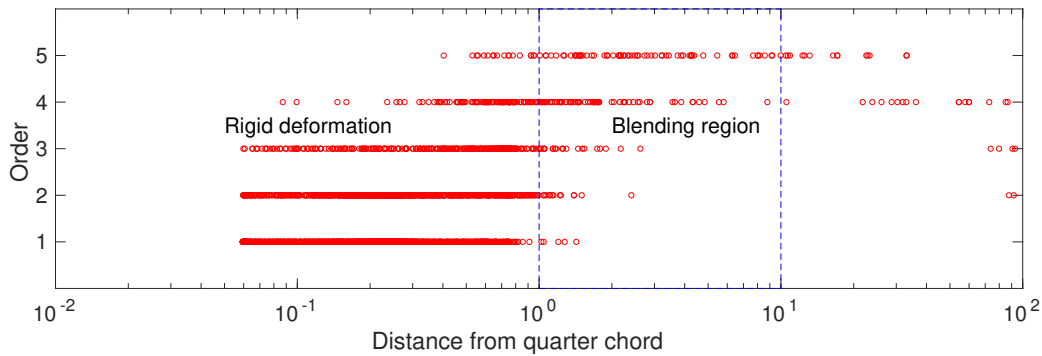
American Institute of Aeronautics and Astronautics

Figure 13. Spatial distribution of the element spatial order at the end of the adaptation process

ments i.e, p-adaptation for unstructured triangular meshes. The adaptation process begins with a coarse viscous mesh with $p = 1$ order elements in the entire domain. The adaptation process is not directly adapting on the flutter Mach number as the quantity is dependent on the both subsystems and requires the evaluation of the coupled adjoint. However, as the current implementation of the coupled solver provides the fluid adjoint only, the adaptation is based on the time-integrated lift.

$$\bar{J} = \int\limits_{0}^{T} L(t)dt. \tag{34}$$

The accurate estimation of the flutter Mach number and the unsteady lift are both affected by the spatial errors in the fluid subsystem. As the governing equation of the structural subsystem is dependent on the lift, adapting on the unsteady lift will directly affect the flutter Mach number evaluation as well. The Mach number chosen for the adaptation cycle is, $M_\infty = 0.345$, which lies in the subcritical regime. The final time chosen for each adaptation iteration is at the end of the first cycle of oscillation in the plunge displacement of the airfoil. Figure 11 shows the conservation of the x-momentum and y-momentum components of the lift adjoint at initial time. The magnitude of the lift adjoint decreases away from the airfoil showing that the output is most sensitive to the residuals on the elements close to the airfoil. Using the lift adjoint, an unsteady error estimate for the output is evaluated and used to adapt the fluid mesh. The total number of degrees of freedom introduced after each adaptive iteration is set by the growth factor which is set to, $f_{tot}=1.2$. The optimized mesh is obtained by subjecting the coarse mesh to four cycles of adaption.

Figure 12 shows the spatial order of interpolation after each adaptive iteration. The higher order elements ($p = 4$ and $p = 5$) introduced in the adaptation process target the elements with the highest error
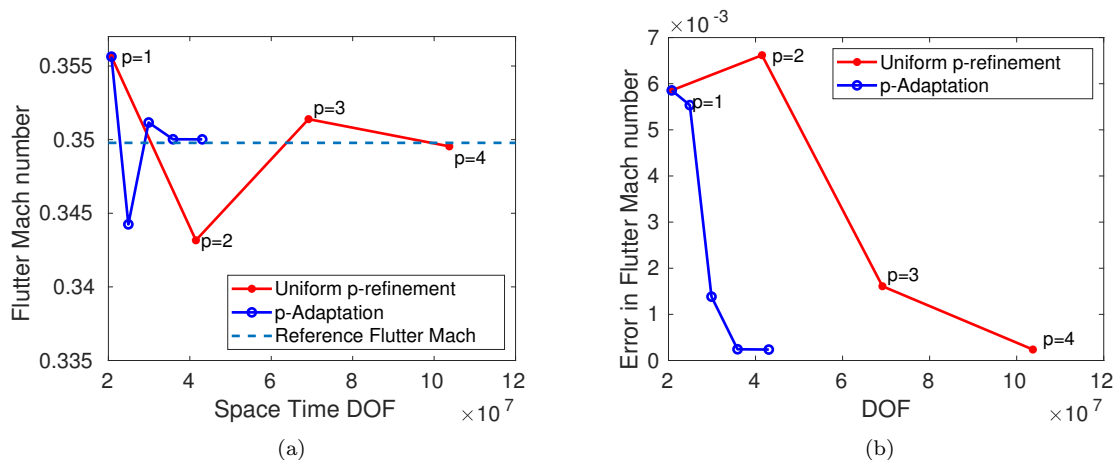

(a)	(b)

Figure 14. Comparison of the flutter boundaries for output-based adaptation to uniform p-refinement.

American Institute of Aeronautics and Astronautics

estimates and lie primarily in the vicinity of the airfoil and inside the blending region, as shown in Figure 13. Adaptation occurring in the blending region seems counter-intuitive as the adjoints on these elements is not as large in magnitude as on the elements inside the rigid deformation region, as seen in Figure 11. The reason behind elements in the blending region being chosen for adaptation also goes back to the definition of the adaptive indicator which is a function of the adjoint and the residual evaluated by projecting the coarse space solution into the fine space. The elements inside the blending region, despite having a lower adjoint magnitude suffer from the errors originating from mesh motion algorithm. This results in a larger residual term in the adaptive indicator. The mesh motion errors become smaller with higher-order approximation[7] but are dominant at lower order approximation of the state, where the adaptation begins. Similar adaptation is not observed in the cantilevered beam case, as the amount of structural displacement is smaller due to the high structural stiffness and added damping.

Figure 14a compares the convergence of the flutter boundary Mach number for the adapted meshes against uniform p-refinement. At every stage of uniform refinement, the spatial order of the elements in the entire domain is increased by one. The reference/truth flutter Mach number, $M_f = 0.3498$ is evaluated on a highly refined viscous mesh with 10492 elements with $p = 4$ elements in the entire spatial domain. The fine mesh is generated by refining the coarse mesh anisotropically. A metric is introduced for the size of each element which is scaled by a factor to obtain the refined mesh. The plot shows the effectiveness of the adaptation process relative to uniform refinement. Figure 14b compares the error in flutter Mach number for the adapted meshes against uniform p refinement. The adapted meshes converge at a faster rate with fewer degrees of freedom, thereby increasing accuracy and reducing computational cost.

VI.   Conclusions

In the paper, the concepts of a high-order partitioned approach are combined with output-based adaptation to provide high-fidelity solutions for fluid-structure interaction problems. The one-dimensional cantilevered beam test case verifies the high-order coupling scheme, IMEX, by demonstrating the expected order of convergence. The two dimensional pitching-plunging NACA 0012 airfoil is also simulated using the high-order coupled solver for which the aeroelastic response is verified at low Mach numbers against Wagner's incompressible aerodynamic model. An adaptive meshing procedure is applied to obtain an accurate drag prediction for the beam case and flutter boundary for the two degree-of-freedom case. The adaptive meshing procedure increases the total computational time of the coupled simulations due to the additional adjoint evaluation by a approximate factor of two. However, the significant benefit of higher accuracy at lower degrees of freedom outweighs the increase in the computational expense. The impact of the mesh motion errors is highlighted significantly in the adapted meshes and a better understanding of the error generated by the mesh motion algorithms is the subject of ongoing research. Overall, the adaptive meshing procedure provides significant increase in the accuracy of unsteady outputs for aeroelastic problems compared to more common adaptation methods, such as uniform refinement.

Acknowledgments

References

[1] Guruswamy, G. P., "Interaction of fluids and structures for aircraft applications," *Computational Structural Mechanics & Fluid Dynamics*, Elsevier, 1988, pp. 1–13.

[2] Hou, G., Wang, J., and Layton, A., "Numerical methods for fluid-structure interactiona review," *Communications in Computational Physics*, Vol. 12, No. 2, 2012, pp. 337–377.

[3] Hübner, B., Walhorn, E., and Dinkler, D., "A monolithic approach to fluid–structure interaction using space–time finite elements," *Computer methods in applied mechanics and engineering*, Vol. 193, No. 23-26, 2004, pp. 2087–2104.

[4] van Zuijlen, A. H., de Boer, A., and Bijl, H., "Higher-order Time Integration Through Smooth Mesh Deformation for 3D Fluid-structure Interaction Simulations," *J. Comput. Phys.*, Vol. 224, No. 1, May 2007, pp. 414–430.

[5] Fidkowski, K. J. and Darmofal, D. L., "Review of Output-Based Error Estimation and Mesh Adaptation in Computational
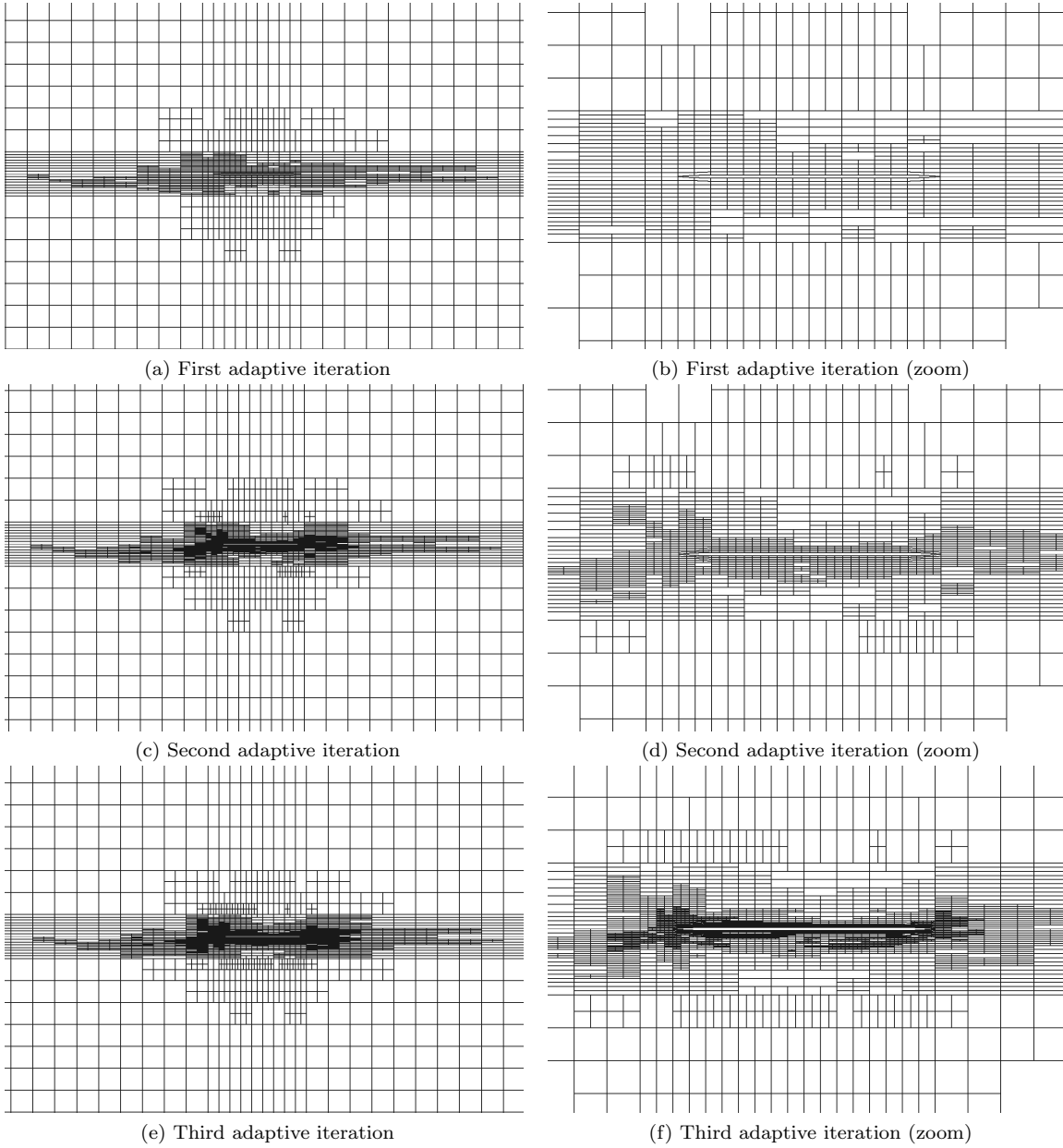
(a) First adaptive iteration

(b) First adaptive iteration (zoom)

(c) Second adaptive iteration

(d) Second adaptive iteration (zoom)

(e) Third adaptive iteration

(f) Third adaptive iteration (zoom)

Figure 15. Successive iterations of hanging node adaptation on the beam test case.

American Institute of Aeronautics and Astronautics

Fluid Dynamics," *American Institute of Aeronautics and Astronautics Journal*, Vol. 49, No. 4, 2011, pp. 673–694.

[6]Persson, P.-O., Bonet, J., and Peraire, J., "Discontinuous Galerkin solution of the Navier–Stokes equations on deformable domains," *Computer Methods in Applied Mechanics and Engineering*, Vol. 198, No. 17-20, 2009, pp. 1585–1595.

[7]Kast, S. M. and Fidkowski, K. J., "Output-based Mesh Adaptation for High Order Navier-Stokes Simulations on Deformable Domains," *Journal of Computational Physics*, Vol. 252, No. 1, 2013, pp. 468–494.

[8]Fidkowski, K. J., Oliver, T. A., Lu, J., and Darmofal, D. L., "p-Multigrid solution of high–order discontinuous Galerkin discretizations of the compressible Navier-Stokes equations," *Journal of Computational Physics*, Vol. 207, 2005, pp. 92–113.

[9]Smith, M. J., Cesnik, C. E. S., and Hodges, D. H., "Evaluation of Some Data Transfer Algorithms for Noncontiguous Meshes," *Journal of Aerospace Engineering*, Vol. 13, No. 2, 2000, pp. 52–58.

[10]Persson, P.-O., Peraire, J., and Bonet, J., "A high order discontinuous Galerkin method for fluid-structure interaction," *18th AIAA Computational Fluid Dynamics Conference*, 2007, p. 4327.

[11]van Zuijlen, A. H. and Bijl, H., "Implicit and explicit higher order time integration schemes for structural dynamics and fluid-structure interaction computations," *Computers & structures*, Vol. 83, No. 2-3, 2005, pp. 93–105.

[12]Froehle, B. and Persson, P.-O., "A high-order discontinuous Galerkin method for fluid–structure interaction with efficient implicit–explicit time stepping," *Journal of Computational Physics*, Vol. 272, 2014, pp. 455–470.

[13]Fidkowski, K. J., "Output-Based Space-Time Mesh Optimization for Unsteady Flows Using Continuous-in-Time Adjoints," *Journal of Computational Physics*, Vol. 341, No. 15, July 2017, pp. 258–277.

[14]Fidkowski, K. J. and Darmofal, D. L., "Review of Output-Based Error Estimation and Mesh Adaptation in Computational Fluid Dynamics," *American Institute of Aeronautics and Astronautics Journal*, Vol. 49, No. 4, 2011, pp. 673–694.

[15]Bisplinghoff, R. L., Ashley, H., and Halfman, R. L., *Aeroelasticity*, Courier Corporation, 2013.

[16]Sanchez, R., L. Kline, H., Thomas, D., Variyar, A., Righi, M., Economon, T., Alonso, J., Palacios, R., Dimitriadis, G., and Terrapon, V., "Assessment of the fluid-structure interaction capabilities for aeronautical applications of the open-source solver SU2." 01 2016, pp. 1498–1529.

[17]Ceze, M. A. and Fidkowski, K. J., "High-order output-based adaptive simulations of turbulent flow in two dimensions," *AIAA Journal*, Vol. 54, No. 9, 2016.